Respiratory Research

RESEARCH

Open Access

Quantitative micro-CT-derived biomarkers elucidate age-related lung fibrosis in elder mice

Davide Buseghin[1,2†], Andrea Grandi[3†], Erica Ferrini[2,3], Gino Villetti[3], Roberta Ciccimarra[4], Nicola Sverzellati[5], Andrea Aliverti[1], Francesca Pennati[1*] and Franco Fabio Stellari[3*]

Abstract

Background Idiopathic Pulmonary Fibrosis (IPF), prevalently affecting individuals over 60 years of age, has been mainly studied in young mouse models. The limited efficacy of current treatments underscores the need for animal models that better mimic an aged patient population. We addressed this by inducing pulmonary fibrosis in aged mice, using longitudinal micro-CT imaging as primary readout, with special attention to animal welfare.

Methods A double bleomycin dose was administered to 18–24 months-old male C57Bl/6j mice to induce pulmonary fibrosis. Bleomycin dosage was reduced to as low as 75% compared to that commonly administered to young (8–12 weeks-old) mice, resulting in long-term lung fibrosis without mortality, complying with animal welfare guidelines. After fibrosis induction, animals received Nintedanib once-daily for two weeks and longitudinally monitored by micro-CT, which provided structural and functional biomarkers, followed by post-mortem histological analysis as terminal endpoint.

Results Compared to young mice, aged animals displayed increased volume, reduced tissue density and function, and marked inflammation. This increased vulnerability imposed a bleomycin dosage reduction to the lowest tested level (2.5 µg/mouse), inducing a milder, yet persistent, fibrosis, while preserving animal welfare. Nintedanib treatment reduced fibrotic lesions and improved pulmonary function.

Conclusions Our data identify a downsized bleomycin treatment that allows to achieve the best trade-off between fibrosis induction and animal welfare, a requirement for antifibrotic drug testing in aged lungs. Nintedanib displayed significant efficacy in this lower-severity disease model, suggesting potential patient stratification strategies. Lung pathology was quantitatively assessed by micro-CT, pointing to the value of longitudinal endpoints in clinical trials.

Keywords Age, Bleomycin model, Lung fibrosis, IPF, Micro-computed tomography, Nintedanib

†Davide Buseghin and Andrea Grandi contributed equally to this work and share first authorship.

*Correspondence:
Francesca Pennati
francesca.pennati@polimi.it
Franco Fabio Stellari
fb.stellari@chiesi.com

[1]Dipartimento di Elettronica, Informazione e Bioingegneria, Politecnico di Milano, Milano, Italy
[2]ANTHEM (AdvaNced Technologies for Human-centrEd Medicine), Spoke 3, Milan, Italy
[3]Experimental Pharmacology & Translational Science Department, Chiesi Farmaceutici S.P.A, Parma, Italy
[4]Department of Veterinary Science, University of Parma, Parma, Italy
[5]Department of Medicine and Surgery, University of Parma, Parma, Italy

Introduction

Idiopathic Pulmonary Fibrosis (IPF) is a chronic and progressive lung disease, characterized by an abnormal deposition of extracellular matrix and fibrotic lesions in the lungs, ultimately leading to respiratory failure [1, 2]. At present, only two drugs, namely Pirfenidone and Nintedanib, have been approved by FDA and EMA as IPF therapeutics. Unfortunately, however, they only delay disease progression in cases of mild to moderate severity [3]. Despite extensive efforts and rigorous preclinical studies aimed at the discovery of new drugs, very few have emerged as potential candidates suitable for translation into efficacious IPF treatments. The recent failure of phase 3 clinical trials for the anti-CTGF antibody pamrevlumab [4] and the autotaxin inhibitor ziritaxestat [5], further underscores the gap, in terms of translatability, between preclinical studies and clinical practice. Part of the difficulties with clinical translation can be ascribed to the oversight of the relationship between IPF and aging in the drug discovery process. Indeed, IPF primarily affects middle-aged to elderly individuals, and its incidence raises with age. Despite this age-related incidence, most antifibrotic drug candidates have been preclinically tested in young animals (8–12 weeks, similar to 18–25 years-old humans) [6], with very few studies conducted in older mice (18–24 months, equivalent to 56–69 years-old humans) [7]. This may be explained by the limited market availability and high cost of aged mice, and the efforts required for the in-house breeding and maintenance of the colonies.

Previous studies on bleomycin (BLM) -induced lung fibrosis in aged mice have provided an incomplete, and sometimes contradictory picture [8–23]. As a general observation, it has been reported that young animals display a faster recovery from BLM treatment, likely due to a shorter duration of fibroblast activation [8], while older mice undergo a more prolonged fibrosis due to their diminished repair capacity [8, 9]. Some studies report more severe fibrosis in elderly mice compared to younger animals [10, 11], while others find comparable levels of fibrosis across different age groups [12]. Interestingly, both young and old fibrotic animals exhibited similar transcriptomics and metabolomics profiles [13, 14], and similarly responded to antifibrotic therapy [15, 16].

Altogether, the above-mentioned studies have left many unaddressed issues, particularly the lack of a detailed characterization of pulmonary fibrosis in aged mice and an incomplete knowledge of the disease temporal progression. These gaps can be covered by in-vivo methodologies such as micro-computed tomography (micro-CT) that allow longitudinal tracking and extrapolation of individual lung fibrosis trajectories. Recently, micro-CT has emerged as a valuable preclinical research tool, capable of longitudinally quantifying disease progression and response to therapeutic treatments in-vivo [24–27]. This could potentially fill many of the gaps in our current understanding of pulmonary fibrosis in older mice.

The aim of the present work was thus to (a) compare the lung characteristics in aged mice (18–24 months) with those in young mice (8–10 weeks old); (b) develop a well-characterized aged mouse model of IPF that uses properly graded amounts of bleomycin to effectively induce lung fibrosis, while ensuring animal welfare; (c) accurately evaluate the response to Nintedanib (NINT) treatment, utilized as a clinical use-approved reference drug. We employed micro-CT to obtain longitudinal structural and functional pulmonary biomarkers, using histological analysis as the final endpoint.

Materials and methods

Experimental animals

The study was conducted in 55 C57Bl/6j male mice, provided by Inovit (San Pietro al Natisone, Italy), which included a group of 42 mice from 18 to 24-month-old (aged mice) and 13 mice from 8 to 10-weeks-old (young mice). Upon their arrival, animals were acclimatized for 20 days to the local vivarium condition (room temperature: 20–24 °C; relative humidity: 40–70%; 12 h light-dark cycle; food and water ad libitum).

All the experiments were conducted according to the guidelines of the Declaration of Helsinki and in compliance with European Directive 2010/63 UE. Italian D.Lgs 26/2014, and the revised "Guide for the Care and Use of Laboratory Animals" (National Research Council Committee, US, 2011). All animal procedures were conducted in an AAALAC (Association for Assessment and Accreditation for Laboratory Animal Care) certified facility at Chiesi Farmaceutici and were authorized by the Italian Ministry of Health with protocol number 742/2022-PR and by the internal AWB (Animal Welfare Body). All required precautions were taken to reduce the animals' suffering or discomfort, and a designated veterinarian or trained technicians assessed pain levels daily using a Visual Analogue Scale (VAS) ranging from 0 to 10. Humane outcomes included dyspnea, weight loss of 20% or more, and a VAS score of 6 or above.

Experimental protocol

The experimental protocol is composed of three distinct stages. The first stage involves a baseline comparison between untreated aged mice and young mice. The second stage is a study to determine the appropriate dosage of bleomycin. The final stage is a pharmacological validation study. The number of mice used in each stage, along with the experimental setup, is summarized in Fig. 1.

a. *Comparison between untreated young and aged.* All mice (42 aged and 13 young) underwent micro-CT

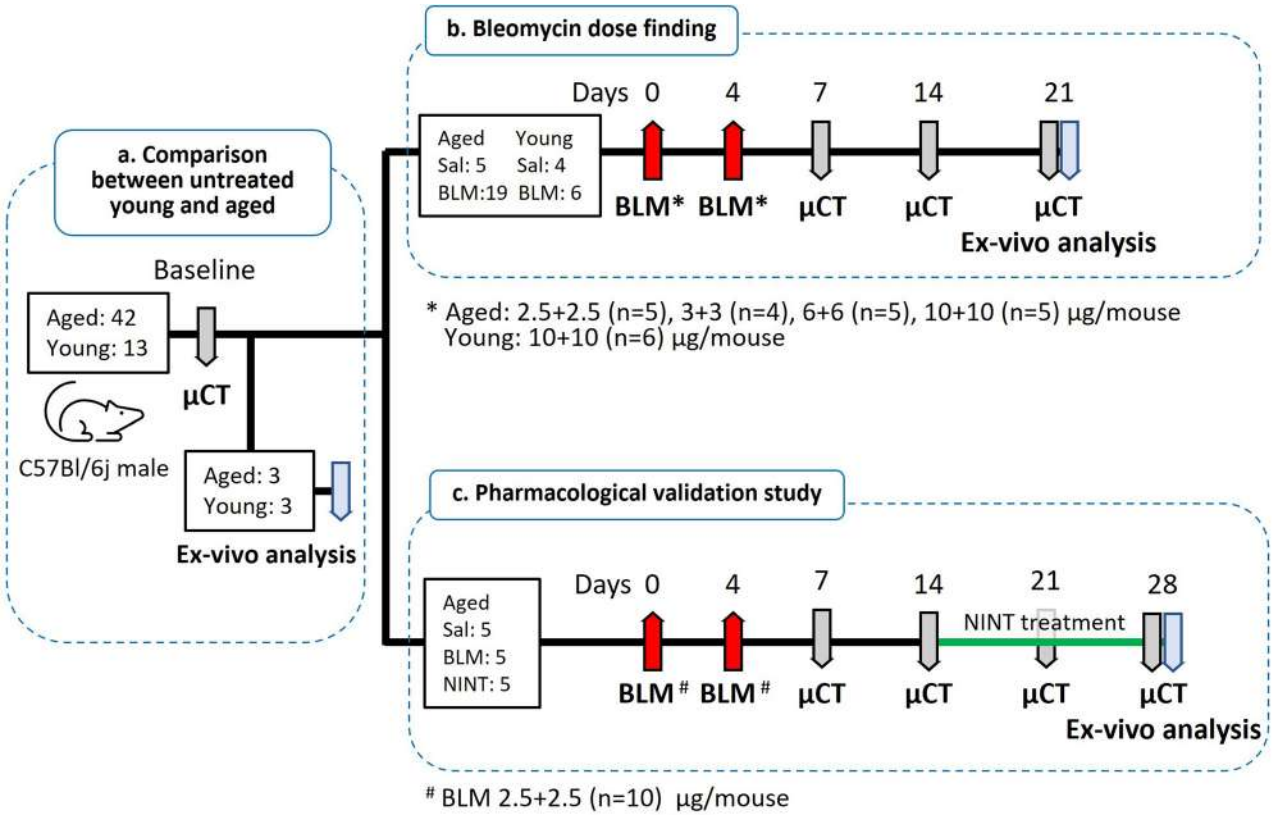

Fig. 1 Experimental protocol and dose finding scale down. Schematic representation of the experimental protocol. (**a**) Comparison between untreated young and aged mice: 55 C57Bl/6j male mice underwent micro-CT at baseline (42 aged and 13 young). 6 animals were sacrificed for histological evaluation. (**b**) Bleomycin- (BLM) dose finding study: 34 mice were treated on day 0 and 4 either with saline ($n=5$ aged and $n=4$ young) or varying doses of BLM ($n=19$ aged and $n=6$ young) by oropharyngeal administration. Mice underwent micro-CT on day 7, 14 and 21 and sacrificed for histological evaluation at the end of the study. (**c**) Pharmacological validation study: 15 aged mice were treated on day 0 and 4 either with saline ($n=5$) or BLM ($n=10$). On day 14, BLM-treated mice were randomized to be treated with Nintedanib ($n=5$) or vehicle ($n=5$). Micro-CT was performed on day 7, 14, 21 and 28 and sacrificed for histological evaluation at the end of the study

at baseline, then 6 animals (3 young and 3 aged) were culled to compare histological assessment for young and aged sham.

b. *Bleomycin dose finding.* 34 mice were randomly selected for the dose finding study. Lung fibrosis was induced in 25 mice (19 aged and 6 young) using Bleomycin (Baxter Oncology GmbH) diluted in 50 µL saline (0.9%) via a double (day 0, 4) oropharyngeal administration, whereas 9 mice served as saline controls (5 aged and 4 young). Briefly, mice were anesthetized with 2.0% isoflurane in oxygen and placed on the intubation platform, hanging by their incisors over a wire. Using a small laryngoscope, the tongue was firmly but gently pulled out with forceps, and with a micropipette the liquid was delivered into the distal part of the oropharynx while the nostrils were gently closed [28, 29].

Since, in our hand, young adult C57Bl/6j male mice receiving a double shot of BLM at 10 µg/mouse developed a sustained lung fibrosis up to 21 days, the same dose scheme (double BLM instillation of 10 µg/mouse) has been initially proposed for aged mice, followed by a scale down of the dose. We tested four different BLM doses on aged mice:

- BLM 10 + 10: 5 aged mice received double BLM administration of 10 µg/mouse;
- BLM 6 + 6: 5 aged mice received double BLM administration of 6 µg/mouse;
- BLM 3 + 3: 4 aged mice received double BLM administration of 3 µg/mouse;
- BLM 2.5 + 2.5: 5 aged mice received double BLM administration of 2.5 µg/mouse;

After double BLM administration at day 0 and 4, we conducted a longitudinal investigation using micro-CT scan at day 7, 14 and 21, which served as the final timepoint for the study. At the endpoint, Bronchoalveolar lavage fluid (BALF) and lungs were harvested for inflammatory cells' measurements and histological analysis

respectively. VAS score and Body Weight were recorded during all the experiment every second day.

c. *Pharmacological validation study.* The pharmacological validation study was conducted with 15 aged mice using the BLM setting selected from the dose finding experiment (double BLM at 2.5 μg/mouse). BLM was administered to 10 mice at day 0 and 4, and saline solution was administered to the other 5 animals at the same timepoints as negative control group. After BLM administration, 5 out of the 10 animals were treated with 60 mg/kg Nintedanib (NINT) p.o. once daily for two weeks from day 14 to day 28 and the remaining 5 mice received the vehicle (1% Tween 80 in water) and were used as negative control group. VAS score and body weight were registered every second day throughout the study. Longitudinal micro-CT has been performed on baseline and on day 7, 14, 21 and 28. At the end-point mice were culled for ex-vivo analyses.

Micro-CT acquisition protocol

Retrospective respiratory gated micro-CT scans were longitudinally acquired at baseline and at day 7, 14, 21, and 28 using a Quantum GX Micro CT scanner (PerkinElmer, Inc. Waltham, MA). To ensure uniformity in respiratory rate (100–120 breath per minute) and depth of ventilation, the mice were administered 2% isoflurane anesthesia. The animals were reclined in supine position on the scanner bed, ensuring that the chest was aligned within the field of view. A region of interest was positioned over the diaphragm for respiratory motion monitoring and gating. Images were acquired with an established and consistent protocol: X-ray tube current 88 μA, X-ray tube voltage 90 kV, and total scan time of 4 min. Over a full 360° gantry rotation, projection images were collected in list-mode every 16.6 ms. The raw data were reconstructed by employing a filtered back-projection algorithm with a Ram-Lak filter. The reconstruction yielded two distinct 3D datasets, corresponding to the end-inspiratory (INSP) and end-expiratory (EXP) phases. Each phase consisted of approximately 900 projections, resulting in a total of 512×512×512 slices. The voxel dimension was 50 μm^3. To ensure data reproducibility, micro-CT is calibrated monthly with phantoms for noise, low contrast, and resolution [30].

Micro-CT image analysis

Lung segmentation was automatically performed by using a deep convolutional neural network (CNN) with U-Net architecture, previously developed and validated by Vincenzi et al. [25, 27], and specifically designed to segment healthy and fibrotic murine lung.

Morphological and densitometric parameters

Lung Volume and Mean Lung Attenuation (MLA) were automatically extracted from the segmented images, and micro-CT derived morphological biomarkers were calculated as reported in Table 1. Aeration compartments (i.e., Normo-, Hypo- and Non-aerated volumes) are defined according to the "HU preclinical ranges" described by Mecozzi et al. [24].

Ventilation maps and functional parameters

To infer regional ventilation, maps of specific gas volume change (ΔSVg) between the inspiration and expiration phase are derived. Specifically, the end-expiratory images were registered to the corresponding end-inspiratory images and subtracted on a pixel-by-pixel basis [26]. ΔSVg provides the change in the amount of air per pixel relative to the mass of tissue between inspiration and expiration. From the ventilation maps, functional parameters, specifically descriptive statistics and ventilation compartments, were derived, using the definitions reposted in Table 1.

Ex vivo lung assessment

Telomere length quantification

All mice were sacrificed by an anesthetic overdose followed by abdominal aortic bleeding; for six sham mice (3 young and 3 aged) a fresh piece of lung was immediately collected and kept frozen at -80 °C until DNA extraction. DNA was extracted and purified using the PureLink Genomic DNA kits (Invitrogen) following the manufacture's instruction for mammalian tissues, and then quantified as ng/ml with a Nanodrop 2000c instrument.

Telomer length was quantified by the Absolute Mouse Telomere Length Quantification qPCR Assay Kit (ScienCell Research Laboratories) by following the manufacturer's instruction and using a mouse genomic DNA provided by the kit supplier as a reference. Results were expressed as mean telomere length per each chromosome end (kilobases, kb) ± SEM.

Bronchoalveolar lavage fluid (BALF) inflammatory cells

BALF was collected by gently washing the lungs three times with 0.6 mL sterile solution (1xHank's balanced salt solution (HBSS) containing 10 mM ethylenediaminetetraacetic acid (EDTA) and 10 mM 4-(2-hydroxyethyl)-1-piperazineethanesulfonic acid (HEPES) with 0.6 ml distilled solution). After BALF samples centrifugation (300 g for 10 min at 4 °C), the resultant cell pellets were resuspended in 0.2 mL of BALF solution. The number of total white blood cells (WBC) and their subpopulations

Table 1 Micro-CT-derived densitometric and functional biomarkers

Name	Description	Unit	Formula
Densitometric Biomarkers			
N_{EXP}	Number of voxels at end expiration	\	Count of lung voxels in exp
Vol_{EXP}	Lung volume at end expiration	apex (mm^3)	$N_{EXP} \cdot$ voxel size
MLA_{EXP}	Mean lung attenuation at end expiration	HU	$\sum_{i=1}^{N_{P02}} (HU)_i / N_{EXP}$
N_{INSP}	Number of lung voxels at end inspiration	\	Count of lung voxels in insp
Vol_{INSP}	Lung volume at end inspiration	apex (mm^3)	$N_{INSP} \cdot$ voxel size
MLA_{INSP}	Mean lung attenuation at end inspiration	HU	$\sum_{i=1}^{N_{P01}} (HU)_i / N_{INSP}$
%Normo-aerated	Normo-aerated lung parenchyma; reflects the extension of no/mild lesions.	%	percent voxels in range [-860, -435]
%Hypo-aerated	Hypo-aerated lung parenchyma; reflects the extension of moderate lesions.	%	percent voxels in range (-435, -121)
%Non-aerated	Non-aerated lung parenchyma; reflects the extension of severe lesions.	%	percent voxels in range [-121, 121]
Functional Biomarkers			
Median ΔSVg	Median of ΔSVg	ml/g	50^{th} percentile of ΔSVg distribution
25^{th} percentile ΔSVg	25^{th} percentile of ΔSVg	ml/g	25^{th} percentile of ΔSVg distribution
%Normal-ventilation	Lung parenchyma with normal ventilation	%	$\Delta SVg \geq \beta$ $SVg_{INSP} \geq \alpha_I$ $SVg_{EXP} \geq \alpha_E$
%Low-ventilation	Lung parenchyma with reduced ventilation, not due to fibrosis	%	$\Delta SVg < \beta$ $SVg_{INSP} \geq \alpha_I$ $SVg_{EXP} \geq \alpha_E$
%Non-ventilation	Lung parenchyma with reduced ventilation due to fibrosis	%	$SVg_{INSP} < \alpha_I$ $SVg_{EXP} < \alpha_E$

ΔSVg, specific gas volume change between inspiration and expiration. α_I and α_E represent the 5^{th} percentile values of the inspiratory and expiratory SVg young basal mean distributions, respectively; β is the 25^{th} percentile of the ΔSVg young basal mean distribution

were counted with an automated cell counter (Dasit XT 1800 J, Sysmex).

Histological analysis

After the sacrifice, lungs were inflated with a cannula through the trachea with 0.6 ml of 10% neutral-buffered formalin and fixed for 24 h. The lungs were dehydrated in graded ethanol series, clarified in xylene and paraffin embedded. Three 5-µm sections were cut with a rotary microtome (Slee Cut 6062; Slee Medical, Mainz, Germany), following the dorsal plane, and stained with Masson's Trichrome (MT), Picrosirius red and Hematoxylin–Eosin. Whole-slide images were acquired by the NanoZoomer S-60 Digital slide scanner (Hamamatsu). The fibrotic lung injury was assessed through Ashcroft scoring system (AS) [31–33] by three independent histopathologists blinded to the experimental design. For each sample, multiple 10X fields were analyzed and morphological changes were graded and classified obtaining an average score.

Immunofluorescent analysis

Immunofluorescent (IF) reactions were conducted on paraffin-embedded sections which underwent deparaffinizion and rehydratation. Antigen retrieval was achieved by exposing the sections to 10 mM citrate buffer pH 6.0, brought to boiling point. After cooling, slides were rinsed in a wash buffer and then incubated in blocking buffer (0.3 M glycine, 5% bovine serum albumin in PBS 1X (Sigma-Aldrich, USA)) for 15 min at room temperature (RT). Then, sections were incubated with primary antibody (Keratin, type II cytoskeletal 8, MABT329 Sigma-Aldrich (1:500)) overnight at 4 °C and with secondary antibody (Goat anti-rat AlexaFluor-488 (ab150157, Abcam)) for 45 min at RT. For negative control, the primary antibody was omitted. After each step, the sections were washed with PBS. Lastly, the nuclei were counterstained with 300 nM of DAPI (Cat#D1306, Invitrogen, USA) solution for 5 min and mounted with ProLong Diamond Antifade Mountant (Cat# S36963, Invitrogen, USA). Fluorescent WSI were acquired using a microscope slide scanner (Olympus VS200, Evident, Japan).

Statistical analysis

Statistical analyses were performed with Prism 10 software (GraphPad Software Inc., San Diego, California, United States) and $p<0.05$ was considered statistically significant. Statistical analysis was performed on densitometric and ventilation parameters, on BALF cells count and histological readouts. Data was assessed for normality via Shapiro-Wilk and Kolmogorov-Smirnov tests and

for homoscedasticity by applying the Brown–Forsythe test. All data, at all experiment stages, fulfilled normality and homoscedasticity. For distinct phases of experiment, different statistics were used.

a. *Comparison between untreated young and aged*: the unpaired Student's t-test was used to measure the difference between groups (aged vs. young) for densitometric and functional parameters obtained through micro-CT.
b. *Bleomycin dose finding study*: densitometric and functional parameters were longitudinally presented and comparison between groups was performed by Two-way ANOVA with Dunnett's multiple comparison's test, which compared each group with aged saline group; differences between timepoints were analyzed with Two-way ANOVA with Sidak's multiple comparison's test comparing 14 and 21 days with 7 days. For BALF cells count and Ashcroft score, Fischer's exact test was used in order to compare the aged saline group with the other groups.
c. *Pharmacological validation study*: densitometric and functional parameters were presented longitudinally. Group comparisons were performed by Two-way ANOVA with Dunnett's multiple comparison's test vs. Vehicle group. Differences between timepoints were analyzed with Two-way ANOVA with Sidak's multiple comparison's test, comparing all timepoints vs. Baseline. The same micro-CT parameters were also expressed as the difference between day 28 and day 14, representing the end and the beginning of the treatment, respectively. Statistical analysis was performed using Fischer's exact test to compare the Vehicle and NINT groups. Fisher's exact test was used to compare the Vehicle group with other groups in term of BALF readouts and Ashcroft score evaluation.

Results

Comparison between untreated young and aged mice

Micro-CT derived biomarkers

Figure 2, based on micro-CT scans and a quantitative analysis of the resulting imaging data, illustrates the structural and functional differences that distinguish the lungs of young and aged mice. A timeline graph delineating the stages of lung development and aging in humans and mice is reported in Fig. 2A for the sake of comparison [6, 7]. Ages are given in years for humans and equivalent week-times for mice. Representative coronal images at end-expiration for both young (8–10 weeks-old) and aged mice (18–24 months-old) are shown in Fig. 2B. A larger and darker lung area with a more flattened diaphragm is clearly visible in the aged mouse. Aged mice display a significant decrease in MLA_{EXP} ($p<0.001$), as well as larger lung volumes during both inspiration and expiration ($p<0.001$; see Table S1) compared to young mice. Ventilation maps (ΔSVg) for young and aged mice are shown in Fig. 2C. The aged mouse, in particular, displays limited well-ventilated regions (blue) and expanded areas with reduced ventilation (red), corresponding to ΔSVg values below 0.2 ml/g. The aged mice group displays a significantly larger portion of the lung involved in mild gas exchange compared to the young animals (%Low Ventilation, $p<0.001$), along with a lower median and 25th percentile of ΔSVg compared to the young animals ($p<0.001$; see Table S1).

Histological assessment

The differences between young and old sham animals revealed by micro-CT, were further investigated by ex-vivo assessments. Histological analysis of lung tissue from aged mice revealed the presence of enlarged alveoli with unique structures, identified as lymphoid aggregates, predominantly located near the airways and the blood vessels. As expected, telomere length in lung cells was observed to be reduced in aged mice compared to their young counterparts (Fig. S1).

Bleomycin dose-finding study

In view of the differences between untreated young and aged mice, BLM doses were scaled down in order to identify the optimal dose for inducing long-term fibrosis, yet compatible with animal welfare. As lung exposure in BLM 10+10 is 31.1±0.8 μg BLM/cm^3 Lung Volume, we calculated the different percentage of reduction in lung exposure for the lower doses. The BLM 6+6 dose led to a mean lung exposure of 18.7±0.7 μg/cm^3, equating to a 40% reduction in lung exposure. The BLM 3+3 dose corresponded to a mean lung exposure of 9.0±0.2 μg/cm^3, which is a 71% reduction. Lastly, the BLM 2.5+2.5 dose resulted in a mean lung exposure of 7.6±0.3 μg/cm^3, indicating a 75% reduction.

Visual analogue scale and body weight

All BLM-treated groups featured a higher Visual Analogue Scale (VAS) compared to saline control mice (Fig. S2A-B), with the most pronounced increase in the highest dose group (BLM 10+10). All aged BLM groups consistently displayed a higher VAS score compared to the young BLM 10+10 group (Fig. S2B). Regarding body weight (Fig. S2C-D), all BLM-treated groups, regardless of age, displayed a body weight decrease compared to baseline values, ranging from about −4% to -15% on day 21. The most substantial body weight loss was observed in the **BLM 10+10** and **BLM 6+6** groups; one aged mouse in the 10+10 group succumbed on day 20 and is represented by an empty dot in the graphs. Similar

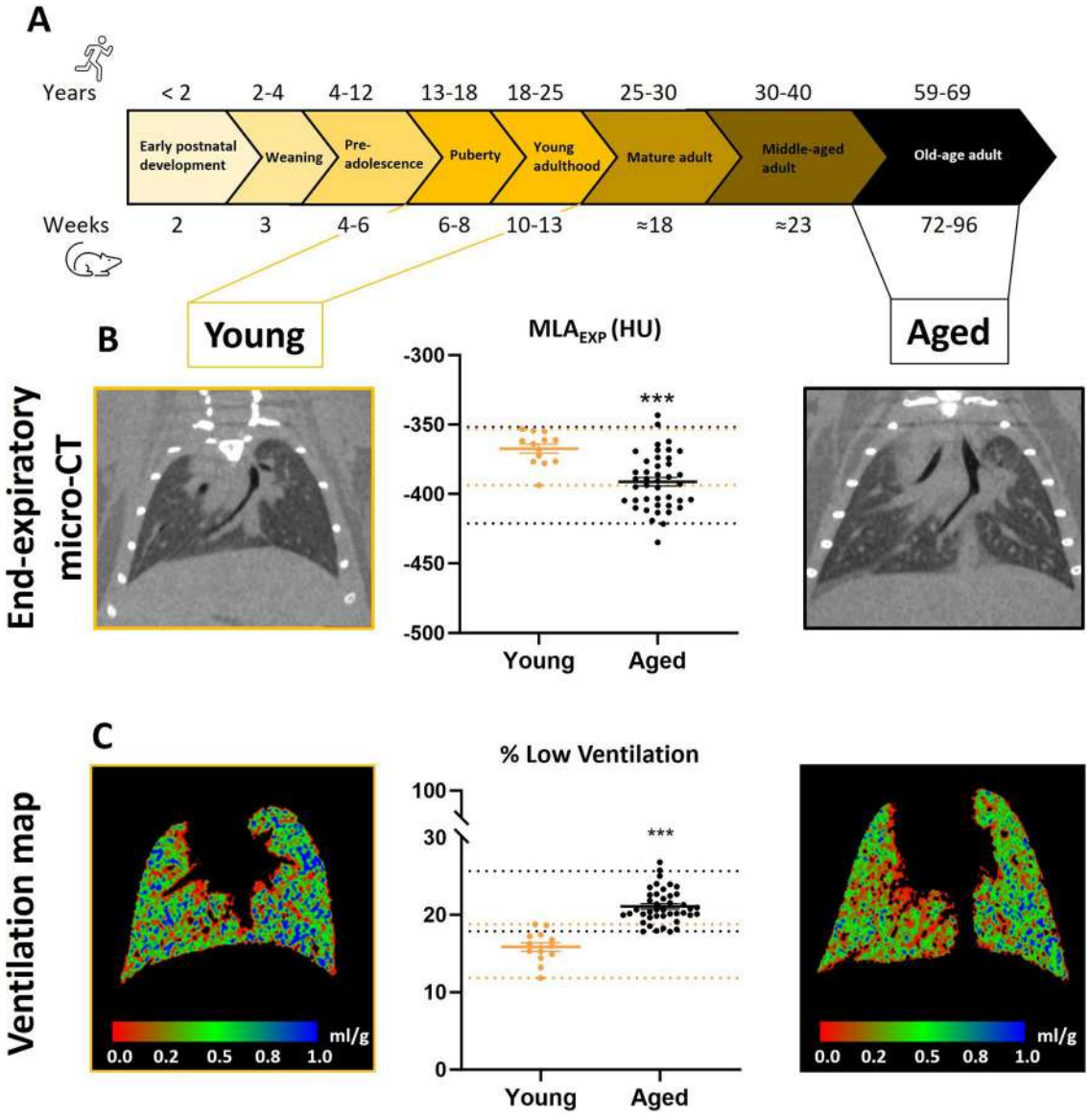

Fig. 2 Comparison between sham young and aged mice. (**A**) Timeline that compares the years of human life to the weeks of mouse life at each stage of development. (**B**) Representative coronal micro-CT images at end-expiration for young (left) and aged (right) mice. Centrally, a scatter plot illustrating mean lung attenuation at end-expiration (MLA_{EXP}) of young (yellow) and aged (back) sham mice. (**C**) Representative coronal ventilation images (indicating changes in specific gas volume, ΔSVg) for the two mice reported in (**B**). Colormap range goes from red (ΔSVg = 0 ml/g) to blue (ΔSVg = 1 ml/g). In the center, the percent extent of low-ventilated lung volume (%Low Ventilation) is presented as a scatter plot for the two groups. For both MLA_{EXP} and %Low vent, the mean ± SEM is reported on the graphs and dotted lines represent 5th and 95th percentiles for each group. Statistical significance between groups was assessed by unpaired Student's t-test (*$p < 0.05$; **$p < 0.01$; ***$p < 0.001$)

to the young BLM 10+10 group, the aged **BLM 3+3** group showed a partial body weight recovery after day 7. A moderate weight loss was observed in the aged **BLM 2.5+2.5** groups, with no sign of recovery till day 21.

Micro-CT-derived biomarkers

Biomarker data extracted from micro-CT scans were also used to evaluate the progression of lung fibrosis in different BLM groups. Longitudinal densitometric (MLA_{EXP} and %Non-aerated) and functional (median ΔSVg and %Non-ventilation) biomarkers measured on days 7, 14, and 21 are shown in Fig. 3 (panels A-D).

The lung density biomarker MLA_{EXP} (Fig. 3A) increased significantly in the aged mice **BLM 10+10** and **BLM 6+6** groups from day 7 to 14 ($p=0.010$, $p=0.006$, respectively) and continued to raise till day 21 ($p<0.001$), with values higher than those of the saline group at day 14 ($p<0.05$) and 21 ($p<0.001$). There was also a significant increase in non-aerated volume (%Non-aerated, Fig. 3B) by day 21 ($p<0.05$ vs. day 7), with significantly

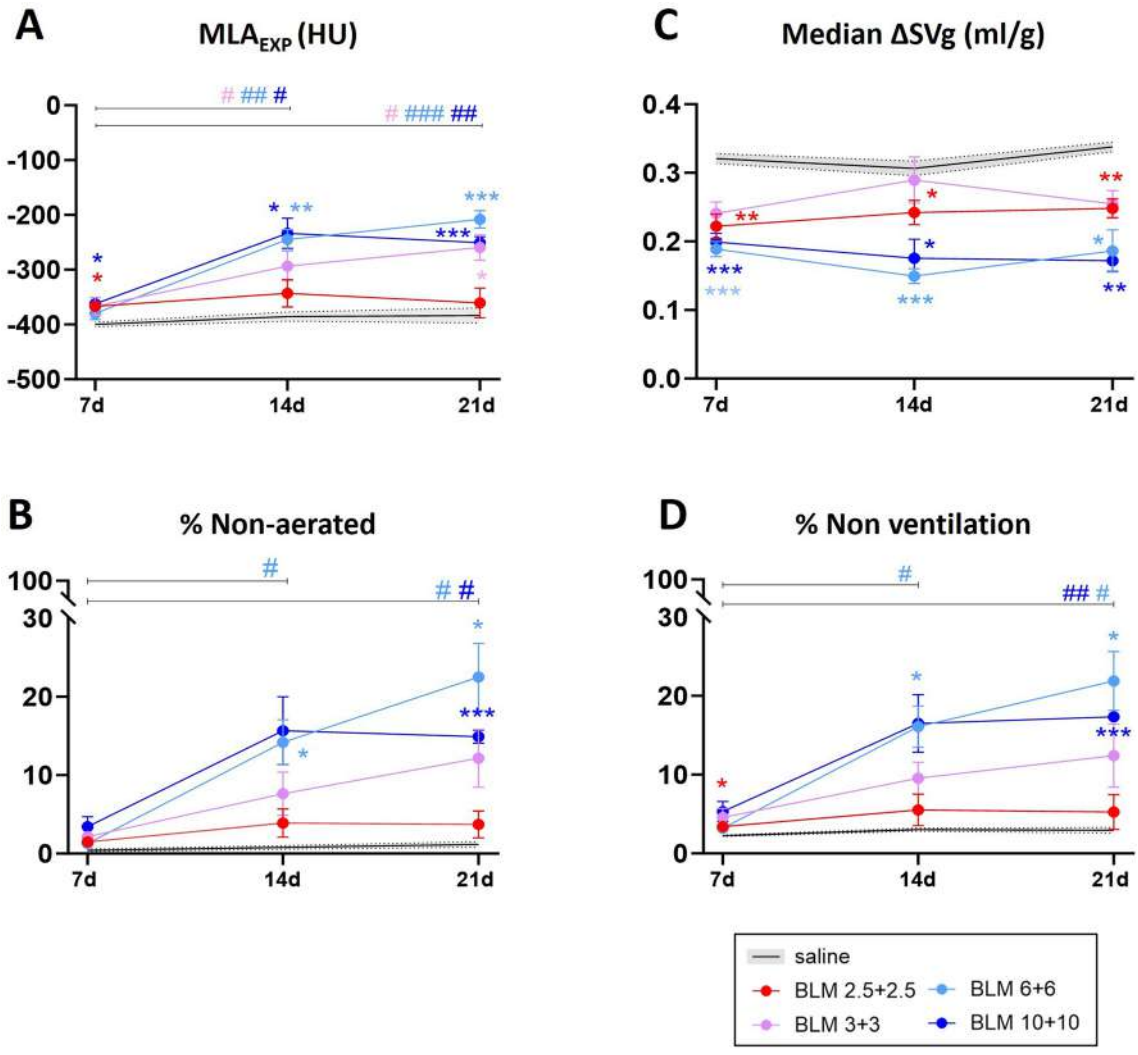

Fig. 3 Bleomycin dose finding experiment: longitudinal densitometric and functional micro-CT derived biomarkers. (**A**-**D**) Densitometric (MLA_{EXP} and %Non-aerated) and functional (median ΔSVg and %Non Ventilation) parameters derived from micro-CT presented longitudinally on day 7, 14 and 21 for aged saline (black), BLM 10 + 10 (blue), BLM 6 + 6 (light blue), BLM 3 + 3 (pink) and BLM 2.5 + 2.5 (red). Data are shown as mean ± SEM. Statistical significance with respect to saline was calculated by two-way ANOVA followed by Dunnett's t post-hoc test (*$p < 0.05$; **$p < 0.01$; ***$p < 0.001$ vs. saline group); statistical significance with respect to day 7 was calculated by two-way ANOVA followed by Šidák post-hoc test (#$p < 0.05$; ##$p < 0.01$; ### $p < 0.001$ 0d vs. 7d). MLA_{EXP}, end-expiratory mean lung attenuation; %Non-aerated, percent extent of non-aerated lung volume; Median ΔSVg, median value of specific gas volume change between the inspiration and expiration; %Non-Ventilation, percent extent of non-ventilated lung volume

higher values compared to the saline control group at the last time-point ($p = 0.022$ and $p < 0.001$ vs. saline, respectively), indicating an extremely severe fibrosis. MLA_{P02} gradually increased in the **BLM 3 + 3** group from day 7 to 14 ($p = 0.038$ vs. day 7) and to day 21 ($p = 0.018$ vs. day 7), reaching values similar to those of the two higher-dose groups at the latter time-point ($p = 0.017$ vs. saline). In contrast, the **BLM 2.5 + 2.5** group maintained relatively stable MLA_{EXP} and %Non-aerated throughout the study with no significant changes over time. Additional density parameters measured on day 21 (see Table S2) confirmed the severe fibrosis observed in the groups treated with the highest BLM doses, with an intermediate condition in the BLM 3 + 3 group, which displayed a significant decrease of %Normo-aerated ($p < 0.001$) and a parallel increase of %Hypo-aerated ($p < 0.01$). A milder fibrotic condition was observed in the BLM 2.5 + 2.5 group, which, as previously indicated by VAS measurements, was the only one that ensured animal welfare and full survival until the end of the experiment (Fig. S2A). Functional biomarker data, specifically median ΔSVg and the extent of non-ventilated regions, are shown in Fig. 3C-D. Median ΔSVg was significantly lower in the **BLM 10 + 10** and **BLM 6 + 6** compared to saline controls at all time-points (day 7: $p < 0.001$ for both groups; day 14: $p = 0.019$ and $p < 0.001$, respectively; day 21: $p = 0.001$ and $p = 0.019$, respectively) (Fig. 3C). The two groups also displayed a significant increase in the extent of

non-ventilated areas from day 7 to day 21 ($p=0.009$ and $p=0.013$, respectively), well above the corresponding values measured in the saline control group on day 14 in the BLM 6+6 group ($p=0.021$) and in both treated groups on day 21 ($p<0.001$, and $p=0.019$, respectively) (Fig. 3D). A reduced median ΔSVg and a progressive, albeit statistically non-significant increase in %Non-ventilation were observed in the **BLM 3+3** group. Despite a fairly modest fibrosis severity, the **BLM 2.5+2.5** group displayed a significant reduction in median ΔSVg compared to saline controls ($p=0.005$ at day 7, $p=0.044$ at day 14, $p=0.002$ at day 21 vs. saline) with minimal alterations in the extent of non-ventilated regions. The additional functional parameters measured on day 21 (see Table S2), confirm a severe ventilation impairment in the highest BLM dose groups, and a milder condition in the BLM 3+3 and 2.5+2.5 groups despite a significant increase of %Low ventilation.

End-of-study evaluations

Representative axial micro-CT images and corresponding ΔSVg maps and histological lung sections for all aged mice BLM-treated groups at the terminal timepoint (day 21) are shown in Fig. 4 (panels A'-A'"). A dose-dependent increase in lung density, characterized by the emergence of patchy high-density areas, particularly pronounced in the left lobe, was observed in the BLM groups. Functional ΔSVg maps (Fig. 4A") confirmed a dose-dependent impairment of lung function with an increased structural deterioration, as indicated by the increase in *red* zones (i.e., areas of reduced ventilation; ΔSVg≈0 ml/g), again particularly evident in the left lobe. These observations were confirmed by the mean distributions of end-expiratory lung density and ΔSVg reported in Fig. 4B-C. In the density histogram (Fig. 4B), a right shift, i.e., towards higher densities that represents a sign of lung damage, is apparent in the BLM-treated groups compared to the saline controls. A secondary peak around 0 HU is observed for the BLM 10+10, BLM 6+6, and BLM 3+3 groups. This peak indicates the presence of lung regions in the lung that are not aerated – a fibrosis sign that increases with the BLM dose. In contrast, only a thickening of the right-side lung tail compared to the saline control distribution was observed in the BLM 2.5+2.5 mice, indicating a modest increase in lung density. Regarding the functional distribution (Fig. 4C), the two higher-dose groups were markedly left-shifted (i.e. towards ΔSVg=0 ml/g), indicating a significant loss of lung function compared to saline controls. On the other hand, the BLM 3+3 and 2.5+2.5 distributions were moderately left-shifted compared to saline, indicating a minor loss in lung function.

Consistent with micro-CT findings, lungs from BLM-treated aged animals displayed varying degrees of confluence, which was practically absent in the saline controls and dose-dependently increased in the BLM groups. The Ashcroft Score significantly increased even in the BLM 2.5+2.5 group compared to saline ($p=0.048$) and further increased in a dose-dependent manner in the other BLM-treated groups (Fig. 4D). Picrosirius Red staining revealed a dosage-dependent increase in collagen deposition as well as an augmented inflammatory infiltrate, which was particularly evident at the highest BLM dose (Fig. S5A-E).

BALF white blood cell counts were found to be elevated in all BLM-treated groups compared to saline controls, with a significant difference in the case of the BLM 6+6 group ($p=0.008$ vs. saline). White blood cell levels followed a bell-shaped dose-effect curve in response to the different BLM treatments: peaking at the 6+6 dose and slightly decreasing upon treatment with the 10+10 dose (Fig. 4E). A similar trend was observed for the BALF lymphocytes (Fig. 4F), with both the BLM 6+6 and the BLM 10+10 groups displaying significantly higher counts compared to the saline controls ($p=0.008$ and $p=0.048$, respectively). Macrophages also increased dose-dependently in aged BLM groups, but the differences did not reach statistical significance (Fig. 4G). An increased percentage of Keratin 8-positive cells was detected by immunofluorescence in all BLM-treated mice, with a less pronounced signal in the BLM 10+10 even if still higher than in saline control animals (Fig. S6 A-E).

The above results confirmed that the BLM 2.5+2.5 treatment, which preserved animal welfare throughout the study, induced a persistent, albeit mild, fibrotic condition, allowing for a longer investigation time extending up to day 28. This dose was thus selected as suitable for antifibrotic drug treatment and pharmacological validation in aged mice.

To support the selection of BLM 2.5+2.5 as the optimal dose for aged mice, we compared aged mice treated with BLM 2.5+2.5 to both young and aged mice treated with BLM 10+10 (Fig. S3). This comparison aimed to highlight the influence of age on fibrosis severity and progression in mice treated with the same BLM dose (10+10), while evaluating if BLM 2.5+2.5 could induce fibrosis in the aged with fewer side effects compared to the 10+10, establishing its effect in aged mice. From day 7 to day 21, mice treated with the standard BLM dose (10+10) displayed a significant time-dependent increase in lung density (MLA_{EXP}, $p=0.001$ for young and $p=0.008$ for aged, at day 21 vs. day 7) and %Non-aerated regions ($p<0.01$ at day 14 and 21 vs. day 7 for both groups), with a steeper increase in the aged group. By day 21, the aged group had significantly higher values compared to the young group ($p=0.037$ for MLA_{EXP} and $p=0.001$ for %Non-aerated). In contrast, aged mice treated with the low BLM dose (2.5+2.5) maintained nearly constant lung density (MLA_{EXP} and %Non-aerated, Fig. S3A-B). Functionally,

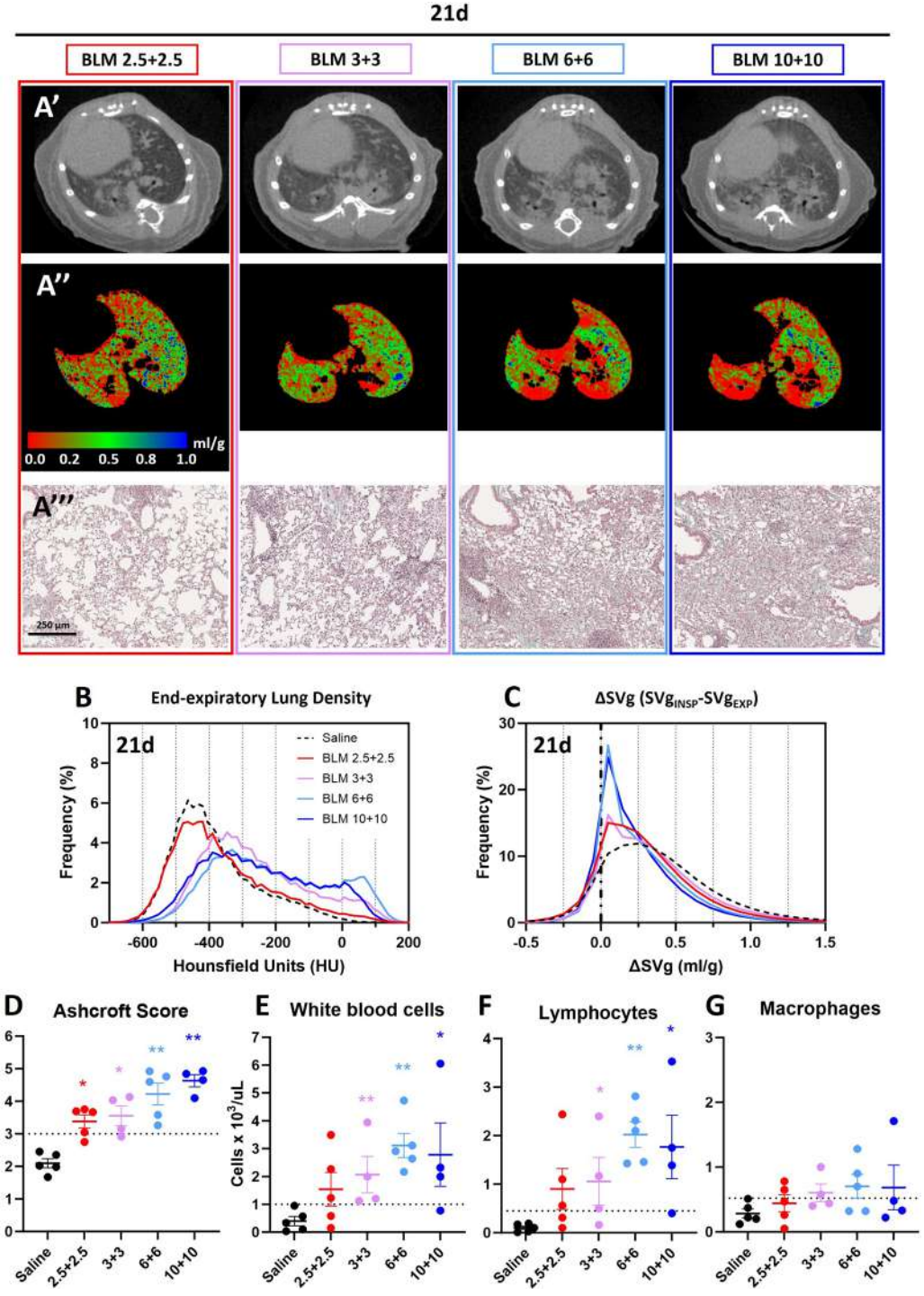

Fig. 4 Bleomycin dose finding experiment: end-of-study evaluations. For all BLM-treated groups representative axial micro-CT slices at end-expiration (**A'**), ventilation maps (inspiratory-expiratory specific gas volume change, ΔSVg) displayed from 0 to 1 ml/g (**A''**), and lung sections (10x magnification, scale bar: 250 µm) stained with Masson's Trichrome (**A'''**) are reported at day 21. From left to right BLM dose increased. (**B**) Mean probability distribution histograms of end-expiratory lung density (Hounsfield Units, HU) and (**C**) ΔSVg on day 21 for the overall group of saline (black, dashed line), BLM 10 + 10 (blue, solid line), BLM 6 + 6 (light blue, solid), BLM 3 + 3 (pink, solid) and BLM 2.5 + 2.5 (red, solid). (**D**) Ashcroft score, (**E**) Bronchoalveolar Lavage Fluid levels of total White Blood Cells, (**F**) Lymphocytes and (**G**) Macrophages are reported individually and as mean ± SEM for each group. Statistical analysis was performed by Fischer's exact test (*$p < 0.05$, **$p < 0.01$, ***$p < 0.001$ vs. saline); the dotted line represents the threshold level utilized for the classification. Additionally, Fischer's exact test was used to compare young and aged saline groups observing significant difference in Ashcroft score (Ashcroft Score about 1 and 2, respectively, $p = 0.048$)

young mice treated with the standard BLM dose (10+10) and aged mice treated with the low BLM dose (2.5+2.5) exhibited similar changes in median ΔSVg, both showing lower values compared to saline controls (Fig. S3C), but the aged BLM 10+10 group experienced a progressive decline, resulting in a lower median ΔSVg at day 21, compared to the young BLM 10+10 group ($p=0.018$). %Non Ventilation (Fig. S3D) showed a slow increase in the young BLM 10+10 group and a marked increase in the aged BLM 10+10 group, with significantly higher values by day 21 ($p<0.001$), while it remained stable in the aged BLM 2.5+2.5 group. Representative axial micro-CT images (Fig. S3E) showed uniform aeration in young saline controls, patchy mild dense areas in aged BLM 2.5+2.5 mice, and more pronounced dense areas in aged and young BLM 10+10 mice, particularly in the left lobe, though the severity was less pronounced in the young. The Ashcroft Score in the young BLM 10+10 mice was higher compared to the aged BLM 2.5+2.5 group ($p=0.048$) and was comparable between the young and the aged BLM 10+10 groups (Fig. S3F). No significant differences were detected in BALF cells counts between the three BLM groups, with a trend towards higher WBCs, lymphocytes and macrophages counts in aged BLM 10+10 mice (Fig. S3G-I).

Pharmacological validation study

In a proof-of-concept pharmacological study, we used the clinically approved Nintedanib (NINT) as a test drug administered daily for a period of 28 days.

VAS and body weight

VAS score and Body Weight showed similar trends for untreated BLM 2.5+2.5 and NINT-treated groups (Fig. S4A-B), with a reduction in Body Weight and an increased VAS score from day 7 to day 28, with an average score of 1.5 for both groups.

Micro-CT derived biomarkers

Representative coronal micro-CT slices with densitometric and functional maps are reported in Fig. 5A-B at the pharmacological treatment baseline (day 14) for saline and BLM 2.5+2.5, and at the end of the study (day 28) for vehicle- and NINT-treated aged mice. On day 14, the saline showed uniform normo-aerated (Fig. 5A, *green regions*), and well-ventilated lungs (Fig. 5B, *green-blue regions*). In contrast, the BLM-treated mouse exhibited extensive hypo-aerated and non-aerated regions (Fig. 5A', *yellow*) matching large non-exchanging regions (Fig. 5B', ΔSVg=0 ml/g; *red*). Regionally, the left lung was mostly non-aerated in the apical region (red) with extensive hypo-aerated regions (yellow), and characterized by no exchange (ΔSVg=0 ml/g; red), while the lower right lung was largely normo-aerated (green), matching extensive low-exchange areas (green) and small fully functional regions (blue). By day 28 (Fig. 5A"), a marked escalation of hypo-aerated areas became apparent in the vehicle-treated mouse (BLM). In contrast, a decrease in hypo-aerated and non-aerated areas, accompanied by a significant increase in normo-aerated areas was observed in the NINT-treated animals. From a functional point of view (Fig. 5B"), the untreated mouse showed a very similar condition with respect to day 14, whereas a clear trend toward a functional recovery of poor ΔSVg exchange regions, with the right lung showing an extended fully functional area, was observed in the NINT-treated mouse.

To study the fibrosis development and the pharmaceutical effect of Nintedanib, we tracked changes from baseline to day 28 for control, vehicle, and treated groups, in term of MLA_{EXP}, %Non-aerated, Median ΔSVg and %Non ventilated (Fig. 5C-F). The saline control group presented minimal variation in densitometric and functional parameters. Conversely, the vehicle group showed increased lung density (MLA_{EXP}) at day 7 ($p=0.030$ vs. baseline and $p=0.031$ vehicle vs. saline) and remained stable until day 28; with a mean of 5.8% non-aerated regions at day 28. Functionally, the vehicle group had a significant reduction in Median ΔSVg with respect to the saline group ($p=0.012$ at day 7, $p=0.042$ at day 14, $p=0.006$ at day 21), and increased %Non ventilation at day 7 ($p=0.036$ vs. saline) without recovery until day 28. No significative differences were observed between vehicle and NINT groups, probably due to high variability in fibrosis extent at day 14 (start of treatment). However, Nintedanib-treated animals showed reduced lung density and improved ventilation from day 14 to day 28.

To evaluate the pharmacological efficacy of Nintedanib, we compared each biomarker from the end to the beginning of treatment (28d – 14d, Fig. 5G-L). Compared to stable fibrosis in the BLM 2.5+2.5+vehicle group, the NINT group showed significant improvement in lung density (reduced MLA_{EXP}; $p=0.048$) and %Non-aerated (reduced %Non-aerated; $p=0.048$). For functional parameters, the NINT group showed non-significant enhancement in Median ΔSVg and reduced %Non-ventilation ($p=0.048$). Changes in micro-CT-derived densitometric and functional parameters confirmed NINT positive effect on lung density (%Normo-aerated) and partial, not-significant improvement in functional parameters such as %Normal ventilation and the 25th percentile of ΔSVg (Sup Table 3). Representative axial micro-CT slices, corresponding ΔSVg maps and histological slices stained with Masson's Trichrome for the BLM 2.5+2.5 vehicle and NINT groups at the end of the study (day 28) confirmed the efficacy of Nintedanib in reducing the fraction of high-density areas and non-ventilated regions, which was particularly evident in the right lower lobe (Fig. 6A'-A'").

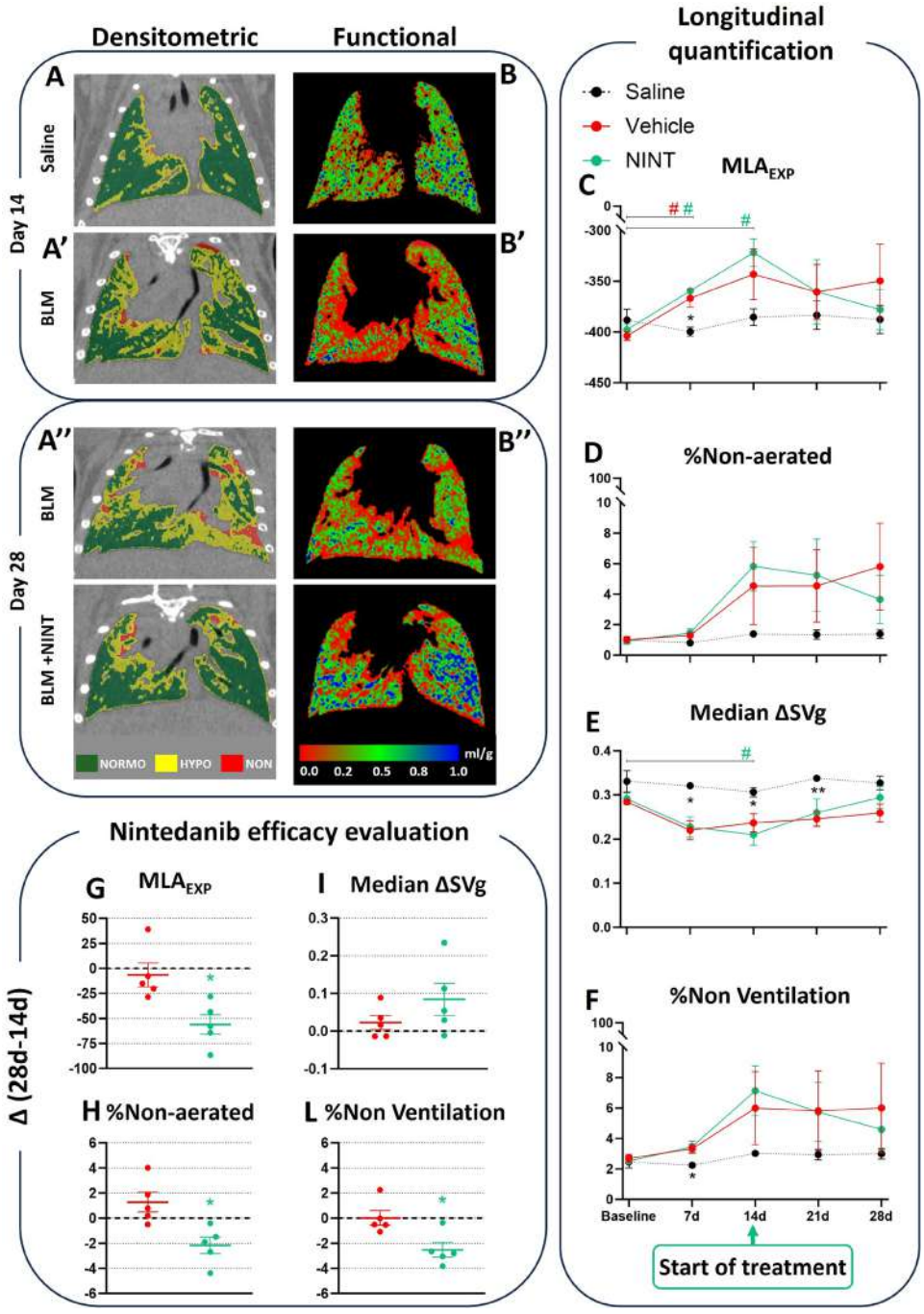

Fig. 5 Pharmacological validation study: longitudinal densitometric and functional micro-CT derived biomarkers. (**A**) Representative coronal micro-CT slices with overlaid aeration compartments at the commencement (day 14) of treatment for saline (**A**) and vehicle (BLM, **A'**) and at its conclusion (day 28) for vehicle (BLM, **A"** middle) and Nintedanib-treated (BLM + NINT, A" bottom) mice. The aeration compartments are color-coded: green for Normo-aerated (Normo), yellow for Hypo-aerated (Hypo), and red for Non-aerated (Non). (**B**) Maps of inspiratory-expiratory specific gas volume change ($\Delta SVg = SVg_{INSP} - SVg_{EXP}$) for the same mice depicted in **A**-**A"**. The range of display is from 0 to 1 ml/g. (**C**) Mean lung density at end-expiration (MLA_{EXP}), (**D**) percent extent of non-aerated compartment (%Non-aerated), (**E**) Median ΔSVg and (**F**) percent extent of non-ventilated lung parenchyma (%Non-ventilation) were presented longitudinally with mean ± SEM at baseline, 7, 14, 21, and 28 days for saline, Vehicle and NINT groups. Statistical significance with respect to Vehicle was calculated by two-way ANOVA followed by Dunnett's t post-hoc test (*$p < 0.05$; **$p < 0.01$; ***$p < 0.001$ vs. Vehicle group); statistical significance with respect to baseline was calculated by two-way ANOVA followed by Šidák post-hoc test (#$p < 0.05$; ##$p < 0.01$; ### $p < 0.001$ 0d vs. baseline). (**G**-**L**) Same parameters of **C**-**F** were, also, presented as difference between end and start of the treatment (28d – 14d) for Vehicle and NINT groups and reported as individual data and mean ± SEM for each group. Statistical significance is determined by Fisher's exact test in order to compare Vehicle with NINT group (*$p < 0.05$); the dotted line represents the threshold level utilized for the classification

These observations were further corroborated by the distribution of lung density and ΔSVg values (Fig. 6B-C). Specifically, a left-shifted density distribution, indicative of a marked reduction of the highest densities, was observed in the NINT treatment group (Fig. 6B). Additionally, the NINT ΔSVg curve appears to be slightly right-shifted with respect to the vehicle curve (Fig. 5C), indicating the presence of overall higher ΔSVg values and a better ventilation in NINT-treated animals.

Consistent with micro-CT findings, the Ashcroft score and WBC counts were significantly increased ($p<0.05$) in the BLM-treated aged mice group compared to saline controls (Fig. 6D-E); lymphocytes and macrophages also increased although not significantly (Fig. 6F-G). None of the above parameters significantly varied in the NINT-treated compared to the vehicle group (Fig. 6D-G).

Picrosirius Red staining revealed higher collagen deposition in the BLM+vehicle group with respect to saline, contrariwise Nintedanib treatment mitigated the increase (Fig. S5F-H). Additionally, BLM 2.5+2.5 increased Keratin 8 expression compared to saline, while Nintedanib reduced the signal (Fig. S6F-H).

An explicative summary of the main findings of the three parts of our study, provided by the different methods and techniques (namely, structural and functional micro-CT imaging and ex-vivo analysis) is presented in in Table 2, which highlights results that align with, and corroborate previous studies on this subject, as well as novel insights gained from the present aged mouse model of lung fibrosis.

Discussion

In this study, we used longitudinal micro-CT imaging to quantitatively evaluate the suitability of 18–24-month-old C57Bl/6j male mice, equivalent to 59–69 years-old human [7], as an animal model of IPF incorporating age-related features into a long-lasting, BLM-induced lung fibrosis. Considering that IPF predominantly affects 65 years-old and elder individuals [2], the inclusion of aging-related factors in preclinical models might offer significant translational advantages in assessing the effectiveness of new antifibrotic therapies [7]. Micro-CT and histological analysis revealed distinct features of the aged compared to the young lungs, including an increased lung volume, diminished tissue density and lung function, as well a marked inflammatory state. Because of these distinctive features, a dose-finding study was performed to determine the most appropriate BLM dosage for inducing lung fibrosis in the aged mice. A 75% reduction of the standard BLM dosage commonly administered to young mice represented the optimal balance between fibrosis' severity and animal welfare, a focal point of our work. A marked attenuation of fibrotic lesions and an improved lung function were brought about in this newly set-up model by Nintedanib, an FDA-approved compound that was used as a reference drug for a pharmacological validation study.

The morphological features distinguishing the aged and the young lung revealed by quantitative micro-CT, namely a lower density and larger volume, are consistent with the airspace enlargement and expanded alveolar ductal radius previously reported as peculiar traits of age-related structural remodeling of the lungs [17–19]. These structural alterations are accompanied by important variations in lung function, as evidenced by the decline in gas exchange during tidal breathing revealed by ventilation maps (reduced ΔSVg and increased %Low ventilation). This kind of functional deterioration has not been observed previously and aligns with the changes in lung mechanics taking place during the aging process, which involve a decrease in elastic recoil pressure and airway resistance as well as an increase in tissue stiffness [20, 21]. Hematoxylin-Eosin staining revealed the presence of perivascular and peribronchial lymphoid aggregates in the lungs of aged mice, a histopathological feature not observed in young animals that is indicative of chronic low-grade inflammation. This observation, along with telomere shortening, may reflect and contribute to genetic instability and susceptibility to various age-related pathologies [14, 22, 23] including lung fibrosis.

To our knowledge, the present study, as the first to report a BLM dose-finding investigation in an aged mice model of BLM-induced lung fibrosis, with longitudinal monitoring of disease progression by micro-CT, addresses a critical gap in the field. The increased vulnerability to BLM observed in aged mice made dose-finding study an essential prerequisite of our work. Accordingly, we reduced the exposure of lung parenchyma to BLM from 0 to 75% of the amount typically administered to young mice (BLM 10+10 and BLM 2.5+2.5, respectively), to set conditions for the establishment of long-term fibrosis with no lethality, i.e., a calibrated experimental model that would be amenable to antifibrotic drug treatments complying with animal welfare guidelines.

We began with the double BLM 10+10 dose, typically administered to young mice, which induced severe body weight loss and VAS changes in aged mice, much more pronounced than in their younger counterpart. Compared to young mice, the 10+10 BLM dose caused a significantly greater severity of fibrosis in aged mice, as evidenced by micro-CT imaging and ex-vivo analyses. Animal's death before day 21 was an adverse event in this group. A similar situation was observed in the BLM 6+6 group, which also displayed severe fibrosis, with a significant weight loss, increased VAS score, high collagen deposition and epithelial injury, potentially leading to animals' decease before day 28. These findings confirmed

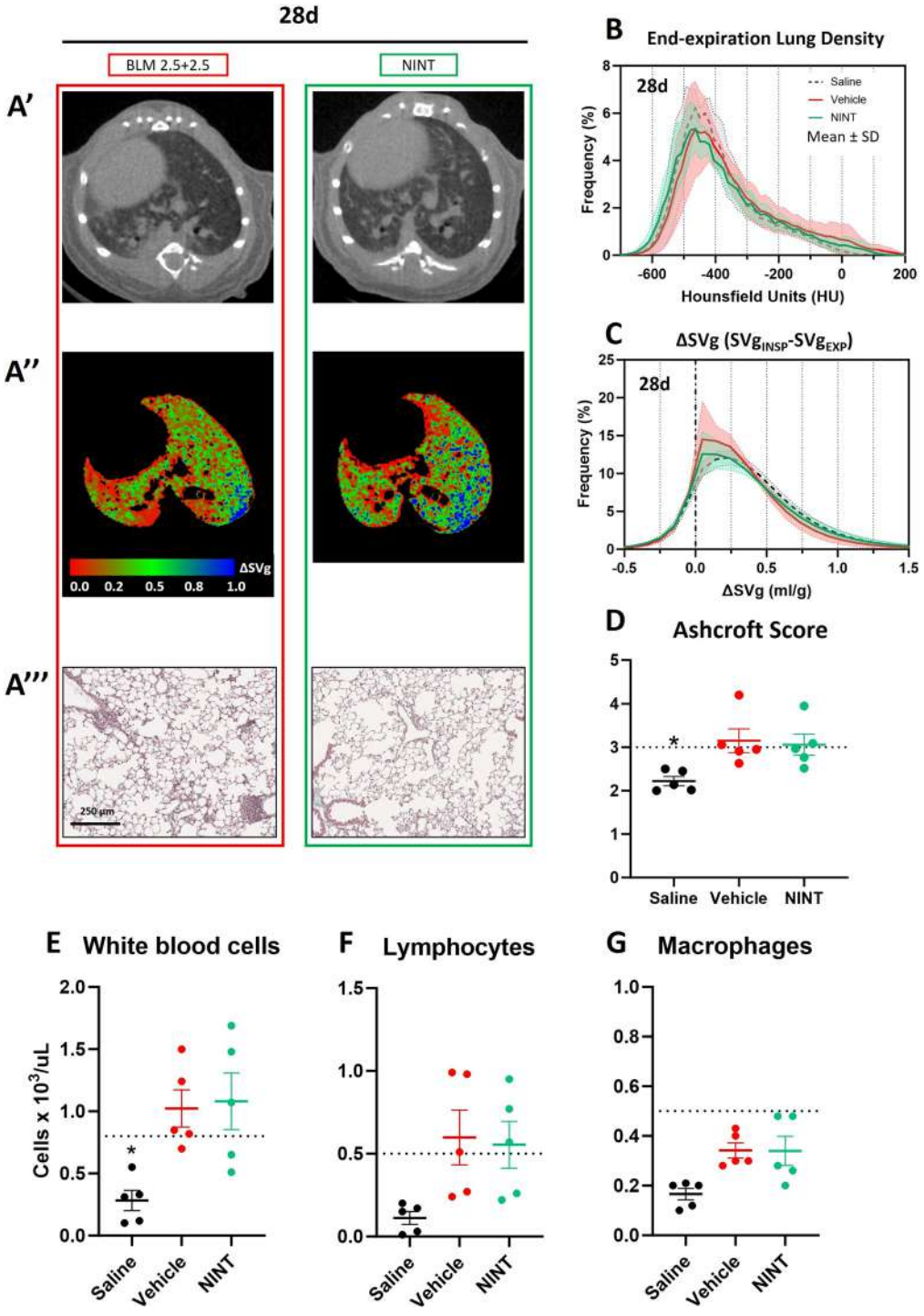

Fig. 6 Pharmacological validation study: end-of-study evaluations. (**A'**) Representative axial micro-CT slices at end-expiration, (**A''**) ventilation maps (inspiratory-expiratory specific gas volume change, $\Delta SVg = SVg_{INSP}\text{-}SVg_{EXP}$) displayed from 0 to 1 ml/g (**A'''**) and lung sections (10x magnification, scale bar: 250 µm) stained with Masson's Trichrome in Vehicle (BLM 2.5 + 2.5) and Nintedanib-treated (NINT) groups, at the end of the study. (**C**) Mean ± SD probability distribution histograms of end-expiratory lung density and (**D**) ΔSVg on day 28 for saline, BLM 2.5 + 2.5 and NINT groups. (**E**) Ashcroft score, (**F**) Bronchoalveolar Lavage Fluid levels of total White Blood Cells, (**G**) Lymphocytes and (**H**) Macrophages are reported individually and as mean ± SEM for each group. In each graph, individual data and mean ± SEM for each group are reported. Statistical analysis is determined using Fisher exact test (*$p < 0.05$ vs. Vehicle); the dotted line represents the threshold level utilized for the classification

Table 2 Main results resume

		Confirmed results	Novel insights
a. Aging lung	**Micro-CT**		
	Structure	Increased lung volume Decreased lung density	-
	Function	-	Lower ventilation
	Ex-vivo analysis	Alveolar enlargement Shorter telomers	Lymphoid aggregates
b. BLM-dose finding	**Animal welfare**	-	Only 2.5 + 2.5 μg/mouse dose ensures animal welfare
	Micro-CT		
	Structure	-	Dose-dependent density increase
	Function	-	Dose-dependent ventilation decline
	Ex-vivo analysis	-	Dose-dependent AS score increase High BALF inflammatory cells for the two highest doses
c. Pharmacological study	**Animal welfare**		2.5 + 2.5 μg/mouse dose is suitable for daily treatment
	Micro-CT		
	Structure	Nint reduces the densest areas	-
	Function	-	Nint slightly improves lung function in aged
	Ex-vivo analysis	Nint reduces fibrosis	

BLM, bleomycin; Nint, Nintedanib; AS Ashcroft Score

the unsuitability of these BLM dosages for long-term modeling and treatment efficacy studies. A progressive fibrosis reaching a mild condition by day 21, yet associated with highly variable VAS scores, was observed with the further reduced BLM 3+3 dose. An exploratory follow-up study extended to day 28 (not shown), conducted on a small group of animals, confirmed a progressive pathology culminating with extensive fibrotic lesions and premature mortality before the intended endpoint, thus making the BLM 3+3 dose also unsuitable. The lowest dose we tested (BLM 2.5+2.5) resulted in a slight increase in lung density and a corresponding decrease in lung functionality, as indicated by micro-CT scans, while having minimal impact on animal welfare; thus, it was deemed optimal. Masson's Trichrome and Picrosirius Red staining confirmed mild collagen deposition and cellular infiltration in the alveolar septa. Additionally, immunofluorescence showed morphological changes, including an increased percentage of Keratin 8-positive cells. This heightened Keratin 8 signal suggests an immediate lung response to injury at this dose, indicating that the epithelial cells are in a "transitional state."

Our findings align with those of previous investigations on the response of young and aged mice to BLM-instillation. Redente et al. [10] reported an increased severity of fibrosis, with higher counts of BALF inflammatory cells and higher levels of pro-inflammatory cytokines, in aged compared to young mice. Similarly, Sueblinvong et al. [11] reported an exacerbated profibrotic phenotype in aged mice, characterized by upregulation of TGF-β and other profibrotic mediators. On the other hand, Hecker et al. [12] and Kato et al. [16] did not observe any significant advantage associated to the use of an aged mouse model of lung fibrosis, and comparable levels of collagen accumulation were detected in both young and aged mice following BLM instillation. Klee et al. [14], with the use of a comparative transcriptomic and proteomic profiling approach, also observed similar molecular changes after BLM administration to aged or young animals. Importantly, however, all the above studies registered rather high mortality rates (from 25 to 45%), raising not only ethical concerns, but also introducing a potential experimental bias due to the premature death of the most severely affected animals, which were obviously excluded from the analysis. Our study aimed to avoid mortality throughout the entire experiment, while maximizing the amount of longitudinal information retrieved from each tested animal, thus complying with current welfare guidelines and the 3Rs (Replacement, Reduction, and Refinement) principles of animal research [34]. Furthermore, unlike the single BLM dose treatment utilized in previous studies, we set out to use a double BLM administration to extend the investigation window up to day 28, i.e., as far as possible from the initial inflammatory peak. Considering that the changes in metabolomic and transcriptomic profiles induced by BLM in aged mice were found to more closely resemble dysregulated pathways associated to human lung fibrosis [13, 14], we believe that our approach, which also takes into account fibrosis progression and animal wellbeing, could improve the translatability of preclinical studies of lung fibrosis. The inclusion in future studies of transcriptomic profiling as an additional biomolecular readout will allow to gain a deeper insight into this model.

In the last part of our study, we investigated the antifibrotic effect of Nintedanib in the BLM (2.5+2.5)-induced lung fibrosis model. We adjusted the therapeutic window to 14–28 days post-BLM administration to circumvent

the initial inflammatory phase [35]. Longitudinal micro-CT analysis showed that NINT treatment, consistent with previous studies [16, 26, 27], significantly reduced fibrotic tissue and non-ventilated regions. Despite these findings, mean lung density and median gas exchange values remained constant throughout the study, likely due to compensatory effects that can mask whole-lung volume data [26, 27]. This highlights the need for caution when interpreting studies that rely solely on forced vital capacity (FVC) as an outcome measure. Moreover, longitudinal micro-CT analysis revealed Nintedanib's impact on fibrosis progression: while static analysis at day 28 showed no significant differences compared to the vehicle group, longitudinal analysis indicated a significant treatment effect when comparing day 28 values to baseline values from day 14. Thus, the combined sensitivity of micro-CT and its capability for longitudinal analyses makes this imaging technique highly effective in evaluating pharmacological treatment efficacy, revealing changes that may be undetectable through terminal analyses or lung function measurements alone. While our micro-CT findings indicate that Nintedanib can effectively reduce even the densest and least functional regions of the lungs in our aged mouse model of low-intensity fibrosis, we did not observe significant changes in the Ashcroft Score, and this was further confirmed by Picrosirius Red staining. This is likely due to the limited number of samples analyzed, which is further complicated by the heterogeneous nature of lung fibrosis, as reflected by the patchy distribution of the densest areas observed on micro-CT. It is worth noting that, while histological analysis is representative of a sampling of the lung parenchyma, micro-CT provides a comprehensive view of the whole lung, enabling a more thorough assessment of the condition. Moreover, the effect of Nintedanib was further validated by Keratin 8 staining, which is primarily expressed in bronchial and alveolar epithelial cells, playing a crucial role in maintaining structural integrity and cellular function. Keratin 8 is also involved in regulating macrophage activity and has been linked to fibrogenesis [36]. Notably, samples from Nintedanib-treated animals did not show transitional epithelial areas, suggesting that Nintedanib may have a reductive effect not only on fibroblasts but also on macrophages and epithelial cells, thereby attenuating the overall fibrotic environment [37].

Similar results were observed in studies performed on young mice [24, 26, 27], suggesting that aging per se is not a key factor determining the ability of Nintedanib to slow-down disease progression. It is important to note, however, that thanks to our preliminary BLM dose-finding study, we applied the NINT treatment to mice displaying relatively mild fibrotic lesions. This condition, which allowed a more sensitive detection of the therapeutic effects of Nintedanib, may resemble the clinical situation of patients with mild fibrosis, thereby enhancing the translational potential of our model. In fact, even though Nintedanib has been found to be generally tolerable and effective in elderly IPF patients [38–40], the incidence of adverse events is likely higher in this population [38]. Indeed, early termination of Nintedanib treatment is more frequent in elderly patients with low body mass index and forced vital capacity [39], who likely suffer from a more severe grade fibrosis. Despite the above-mentioned challenges, NINT's efficacy in mitigating lung fibrosis progression has been found to be consistent across different age groups [16]. This uniformity of therapeutic response, along with the present findings, highlight the potential of Nintedanib as an IPF treatment option for various age groups, but also underlines the importance of taking into account age and disease severity, and thus an accurate patient stratification in clinical trials.

From a methodological perspective, the value of longitudinal micro-CT as a non-invasive imaging tool is well-recognized. In fact, micro-CT has been shown to enable the longitudinal characterization of lung morphology and function, as well as the investigation of fibrosis development and response to antifibrotic treatments in various young mice animal models [24–27, 41]. In this study, we extended the application of micro-CT analysis to aged mice, thus further documenting the high translatability and versatility of an imaging tool that can expand our understanding of age-related changes associated to BLM-induced lung fibrosis. A key aspect of our study was the integration of morphological and functional biomarkers obtained from micro-CT scans, which were found to be highly consistent, thus reinforcing the notion that structural parenchymal alterations directly impact on lung function. These findings point to micro-CT as a key tool for drug discovery-oriented preclinical studies; a tool that significantly reduces the number of experimental animals and contributes to bridging the translational gap to clinical studies, thereby enhancing the potential for the development of novel effective therapeutic strategies.

Despite the conceptual and methodological insights, it provided, this study has some potential limitations. First of all, the use of aged (78 weeks-old) mice might be challenging because of their high cost and limited market availability, with increased maintenance costs due to the need to be periodically separated one from the other. Furthermore, the high variability and limited sample size in the BLM-treated aged groups complicated the task of determining an optimal BLM dosage. Despite the potential of higher doses to induce severe fibrosis, their impact on animal welfare made them unfeasible. As a result, we administered a dosage that only resulted in mild fibrosis, which may have limited the observable therapeutic effects of Nintedanib. Another potential limitation,

despite the detailed functional information on fibrosis development and response to treatment provided by micro-CT, is the lack of a direct assessment of terminal respiratory mechanics. We decided not to perform this kind of analysis because of its invasive nature and the inherent risk of further exacerbating animal-related variability.

Therefore, although the aged mice model of BLM-induced fibrosis may not be readily applicable to primary drug screening, it nevertheless introduces age-dependent features into an animal model of lung fibrosis, thereby enhancing its translational potential, especially with regard to the management of IPF in elderly human populations. Further studies and, particularly, clinical trials with longitudinal endpoints, will be required to confirm these expectations and to verify their relevance in the realm of clinical practice.

Abbreviations

IPF	Idiopathic Pulmonary Fibrosis
BLM	Bleomycin
micro-CT	Micro Computed Tomography
NINT	Nintedanib
BALF	Bronchoalveolar lavage fluid
INSP	Inspiratory
EXP	Expiratory
CNN	Convolutional Neural network
MLA	Mean Lung Attenuation
HU	Hounsfield Units
ΔSVg	Specific gas volume difference
SVg	Specific gas volume
HBSS	Hank's balanced salt solution
EDTA	Ethylenediaminetetraacetic acid
WBC	White blood cells
MT	Masson's Trichrome
AS	Ashcroft Score
IF	Immunofluorescent
ANOVA	Analysis of variance
FVC	Forced Vital Capacity

Supplementary Information

The online version contains supplementary material available at https://doi.org/10.1186/s12931-024-03006-7.

Supplementary Material 1

Supplementary Material 2

Acknowledgements
The authors thank Prof. Simone Ottonello for the critical revision of the manuscript.

Author contributions
DB, AG, EF and FFS conceived and designed the research. AG and EF performed in vivo experiments. RC performed histological analysis. DB and FP analyzed data. DB, AG, EF, FP, AA and FFS interpreted results. DB, AG, EF and FP prepared figures. DB, AG, FP and FFS drafted the manuscript. EF, AA, GV and NS edited and revised the manuscript. All authors approved the final version of the manuscript.

Funding
This study was fully supported by Chiesi Farmaceutici S.p.A. and by the National Plan for NRRP Complementary Investments (PNC, established with the decree-law 6 May 2021, n. 59, converted by law n. 101 of 2021) in the call for the funding of research initiatives for technologies and innovative trajectories in the health and care sectors (Directorial Decree n. 931 of 06-06-2022) - project n. PNC0000003 - AdvaNced Technologies for Human-centrEd Medicine (project acronym: ANTHEM). This work reflects only the authors' views and opinions, neither the Ministry for University and Research nor the European Commission can be considered responsible for them.

Data availability
No datasets were generated or analysed during the current study.

Declarations

Ethics approval and consent to participate
Not applicable.

Consent for publication
Not applicable.

Competing interests
FFS, AG, EF and GV are employees of Chiesi Farmaceutici S.p.A., that supported the research work. The remaining authors declare that the research was conducted in the absence of any commercial or financial relationships that could be construed as a potential conflict of interest.

Received: 8 July 2024 / Accepted: 7 October 2024
Published online: 30 October 2024

References

1. Raghu G, Remy-Jardin M, Myers JL, Richeldi L, Ryerson CJ, Lederer DJ, et al. Diagnosis of idiopathic pulmonary fibrosis. An Official ATS/ERS/JRS/ALAT Clinical Practice Guideline. Am J Respir Crit Care Med. 2018;198:e44–68.
2. Podolanczuk AJ, Thomson CC, Remy-Jardin M, Richeldi L, Martinez FJ, Kolb M, et al. Idiopathic pulmonary fibrosis: state of the art for 2023. Eur Respir J. 2023;61:2200957.
3. Trachalaki A, Irfan M, Wells AU. Pharmacological management of idiopathic pulmonary fibrosis: current and emerging options. Expert Opin Pharmacother. 2021;22:191–204.
4. Raghu G, Richeldi L, Fernández Pérez ER, De Salvo MC, Silva RS, Song JW et al. Pamrevlumab for Idiopathic Pulmonary Fibrosis: the ZEPHYRUS-1 Randomized Clinical Trial. JAMA Published Online May 19, 2024.
5. Maher TM, Ford P, Brown KK, Costabel U, Cottin V, Danoff SK, et al. Ziritaxestat, a novel autotaxin inhibitor, and lung function in idiopathic pulmonary fibrosis: the ISABELA 1 and 2 randomized clinical trials. JAMA. 2023;329:1567–78.
6. Bärnthaler T, Ramachandra AB, Ebanks S, Guerrera N, Sharma L, Dela Cruz CS, et al. Developmental changes in lung function of mice are independent of sex as a biological variable. Am J Physiol Lung Cell Mol Physiol. 2024;326:L627–37.
7. Jenkins RG, Moore BB, Chambers RC, Eickelberg O, Königshoff M, Kolb M, et al. An official American thoracic Society Workshop Report: Use of Animal models for the Preclinical Assessment of potential therapies for pulmonary fibrosis. Am J Respir Cell Mol Biol. 2017;56:667–79.
8. Caporarello N, Meridew JA, Jones DL, Tan Q, Haak AJ, Choi KM, et al. PGC1α repression in IPF fibroblasts drives a pathologic metabolic, secretory and fibrogenic state. Thorax. 2019;74:749–60.
9. Weckerle J, Mayr CH, Fundel-Clemens K, Lämmle B, Boryn L, Thomas MJ, et al. Transcriptomic and proteomic changes driving Pulmonary Fibrosis Resolution in Young and Old mice. Am J Respir Cell Mol Biol. 2023;69:422–40.
10. Redente EF, Jacobsen KM, Solomon JJ, Lara AR, Faubel S, Keith RC, et al. Age and sex dimorphisms contribute to the severity of bleomycin-induced lung injury and fibrosis. Am J Physiol Lung Cell Mol Physiol. 2011;301:L510–8.
11. Sueblinvong V, Neujahr DC, Mills ST, Roser-Page S, Ritzenthaler JD, Guidot D, et al. Predisposition for disrepair in the aged lung. Am J Med Sci. 2012;344:41–51.
12. Hecker L, Logsdon NJ, Kurundkar D, Kurundkar A, Bernard K, Hock T, et al. Reversal of persistent fibrosis in aging by targeting Nox4-Nrf2 redox imbalance. Sci Transl Med. 2014;6:231ra47.
13. Weckerle J, Picart-Armada S, Klee S, Bretschneider T, Luippold AH, Rist W, et al. Mapping the metabolomic and lipidomic changes in the bleomycin

model of pulmonary fibrosis in young and aged mice. Dis Model Mech. 2022;15:dmm049105.
14. Klee S, Picart-Armada S, Wenger K, Birk G, Quast K, Veyel D, et al. Transcriptomic and proteomic profiling of young and old mice in the bleomycin model reveals high similarity. Am J Physiol Lung Cell Mol Physiol. 2023;324:L245–58.
15. Wollin L, Distler JHW, Redente EF, Riches DWH, Stowasser S, Schlenker-Herceg R, et al. Potential of nintedanib in treatment of progressive fibrosing interstitial lung diseases. Eur Respir J. 2019;54:1900161.
16. Kato K, Shin YJ, Palumbo S, Papageorgiou I, Hahn S, Irish JD, et al. Leveraging ageing models of pulmonary fibrosis: the efficacy of nintedanib in ageing. Eur Respir J. 2021;58:2100759.
17. Huang K, Rabold R, Schofield B, Mitzner W, Tankersley CG. Age-dependent changes of airway and lung parenchyma in C57BL/6J mice. J Appl Physiol (1985). 2007;102:200–6.
18. Schulte H, Mühlfeld C, Brandenberger C. Age-related structural and functional changes in the mouse lung. Front Physiol. 2019;10:1466.
19. Quirk JD, Sukstanskii AL, Woods JC, Lutey BA, Conradi MS, Gierada DS et al. Experimental evidence of age-related adaptive changes in human acinar airways. J Appl Physiol (1985). 2016; 120: 159–165.
20. Elliott JE, Mantilla CB, Pabelick CM, Roden AC, Sieck GC. Aging-related changes in respiratory system mechanics and morphometry in mice. Am J Physiol Lung Cell Mol Physiol. 2016;311:L167–76.
21. Veldhuizen RAW, McCaig LA, Pape C, Gill SE. The effects of aging and exercise on lung mechanics, surfactant and alveolar macrophages. Exp Lung Res. 2019;45:113–22.
22. Calyeca J, Balderas-Martínez YI, Selman M, Pardo A. Transcriptomic profile of the mice aging lung is associated with inflammation and apoptosis as important pathways. Aging. 2021;13:12378–94.
23. Ruiz A, Flores-Gonzalez J, Buendia-Roldan I, Chavez-Galan L. Telomere Shortening and its Association with Cell Dysfunction in Lung diseases. Int J Mol Sci. 2021;23:425.
24. Mecozzi L, Mambrini M, Ruscitti F, Ferrini E, Ciccimarra R, Ravanetti F, et al. In-vivo lung fibrosis staging in a bleomycin-mouse model: a new micro-CT guided densitometric approach. Sci Rep. 2020;10:18735.
25. Vincenzi E, Fantazzini A, Basso C, Barla A, Odone F, Leo L, et al. A fully automated deep learning pipeline for micro-CT-imaging-based densitometry of lung fibrosis murine models. Respir Res. 2022;23:308.
26. Pennati F, Leo L, Ferrini E, Sverzellati N, Bernardi D, Stellari FF, et al. Micro-CT-derived ventilation biomarkers for the longitudinal assessment of pathology and response to therapy in a mouse model of lung fibrosis. Sci Rep. 2023;13:4462.
27. Buccardi M, Ferrini E, Pennati F, Vincenzi E, Ledda RE, Grandi A, et al. A fully automated micro–CT deep learning approach for precision preclinical investigation of lung fibrosis progression and response to therapy. Respir Res. 2023;24:126.
28. Ruscitti F, Ravanetti F, Bertani V, Ragionieri L, Mecozzi L, Sverzellati N, et al. Quantification of Lung Fibrosis in IPF-Like Mouse Model and pharmacological response to treatment by Micro-computed Tomography. Front Pharmacol. 2020;11:1117.
29. Ferrini E, Mecozzi L, Corsi L, Ragionieri L, Donofrio G, Stellari FF. Alfaxalone and Dexmedetomidine as an alternative to gas anesthesia for Micro-CT lung imaging in a Bleomycin-Induced Pulmonary Fibrosis Murine Model. Front Vet Sci. 2020;7:588592.
30. Mambrini M, Mecozzi L, Ferrini E, Leo L, Bernardi D, Grandi A, et al. The importance of routine quality control for reproducible pulmonary measurements by in vivo micro-CT. Sci Rep. 2022;12:9695.
31. Ashcroft T, Simpson JM, Timbrell V. Simple method of estimating severity of pulmonary fibrosis on a numerical scale. J Clin Pathol. 1988;41:467–70.
32. Hübner RH, Gitter W, El Mokhtari NE, Mathiak M, Both M, Bolte H, et al. Standardized quantification of pulmonary fibrosis in histological samples. Biotechniques. 2008;44:507–17.
33. Grandi A, Ferrini E, Mecozzi L, Ciccimarra R, Zoboli M, Leo L, et al. Indocyanine-enhanced mouse model of bleomycin-induced lung fibrosis with hallmarks of progressive emphysema. Am J Physiol Lung Cell Mol Physiol. 2023;324:L211–27.
34. Wadman M. FDA no longer has to require animal testing for new drugs. Science. 2023;379:127–8.
35. Khalajzeyqami Z, Grandi A, Ferrini E, Ravanetti F, Leo L, Mambrini M, et al. Pivotal role of micro-CT technology in setting up an optimized lung fibrosis mouse model for drug screening. PLoS ONE. 2022;17:e0270005.
36. Wang F, Ting C, Riemondy KA, Douglas M, Foster K, Patel N, et al. Regulation of epithelial transitional states in murine and human pulmonary fibrosis. J Clin Investig. 2002;133:e165612.
37. Yang Y, Wang X, Zhang J. Pirfenidone and Nintedanib attenuate pulmonary fibrosis in mice by inhibiting the expression of JAK2. J Thorac Disease. 2024;16:1128–40.
38. Komatsu M, Yamamoto H, Ichiyama T, Kawakami S, Uehara T, Yoshikawa Y, et al. Tolerability of nintedanib in the elderly with idiopathic pulmonary fibrosis: a single-center retrospective study. PLoS ONE. 2022;17:e0262795.
39. Uchida Y, Ikeda S, Sekine A, Katano T, Tabata E, Oda T, et al. Tolerability and safety of nintedanib in elderly patients with idiopathic pulmonary fibrosis. Respir Investig. 2021;59:99–105.
40. Mondoni M, Alfano F, Varone F, Muscato G, Conti C, Saderi L, et al. Observational, Multicenter Study on the efficacy, tolerability, and Safety of Nintedanib in patients with idiopathic pulmonary fibrosis older than 80 years. Respiration. 2023;102:25–33.
41. Buccardi M, Grandi A, Ferrini E, Buseghin D, Villetti G, Civelli M, et al. Micro-CT-assisted identification of the optimal time-window for antifibrotic treatment in a bleomycin mouse model of long-lasting pulmonary fibrosis. Sci Rep. 2024;14:14792.

Publisher's note